

Budding transition of asymmetric two-component lipid domains

Jean Wolff*

Institut Charles Sadron, UPR22-CNRS 23, rue du Loess BP 84047, 67034 Strasbourg Cedex, France

Shigeyuki Komura†

*Department of Chemistry, Graduate School of Science and Engineering,
Tokyo Metropolitan University, Tokyo 192-0397, Japan*

David Andelman‡

*Raymond and Beverly Sackler School of Physics and Astronomy,
Tel Aviv University, Ramat Aviv, Tel Aviv 69978, Israel and
CAS Key Laboratory of Theoretical Physics, Institute of Theoretical Physics,
Chinese Academy of Sciences, Beijing 100190, China*

(Dated: July 17, 2016)

We propose a model that accounts for the budding transition of asymmetric two-component lipid domains, where the two monolayers (leaflets) have different average compositions controlled by independent chemical potentials. Assuming a coupling between the local curvature and local lipid composition in each of the leaflets, we discuss the morphology and thermodynamic behavior of asymmetric lipid domains. The membrane free-energy contains three contributions: the bending energy, the line tension, and a Landau free-energy for a lateral phase separation. Within a mean-field treatment, we obtain various phase diagrams containing fully budded, dimpled, and flat states as a function of the two leaflet compositions. The global phase behavior is analyzed, and depending on system parameters, the phase diagrams include one-phase, two-phase and three-phase regions. In particular, we predict various phase coexistence regions between different morphologies of domains, which may be observed in multi-component membranes or vesicles.

I. INTRODUCTION

The cytoplasmic membrane separates the living cell from its extra-cellular surroundings, while other intra-cellular membranes compartmentalize cellular organelles. Biomembranes are constructed from two monolayers (leaflets) in a back-to-back arrangement, and are in general asymmetric in their lipids composition [1, 2]. For example, in human red blood cells, the inner cytoplasmic leaflet is composed mostly of phosphatidylethanolamine (PE) and phosphatidylserine (PS), while the outer cytoplasmic leaflet is composed of phosphatidylcholine (PC), sphingomyelin (SM) and a variety of glycolipids [3, 4]. The asymmetric nature of the cell membrane plays a key role in a variety of cellular processes such as endocytosis [5], vesicle budding and trafficking [6]. Furthermore, in living cells, the composition asymmetry is an active and energy-consuming process. It is maintained by several membrane proteins such as flippase and floppase that allow lipids to exchange between the two leaflets with the aid of adenosine triphosphate (ATP) [7].

In artificial multi-component lipid bilayers, the two membrane leaflets can undergo a lateral phase separation. Several authors made the connection between such a phase separation in artificial membranes and existence of small dynamic domains (“rafts”) in biological mem-

branes [8]. It should be noted, however, the size of rafts in biological membranes are expected to be in the range of 10–100 nm [9, 10]. Rafts are believed to be enriched mixtures of cholesterol and SM in a liquid-ordered phase (L_o), embedded in a background of a liquid-disordered phase (L_d). Despite the lack of an ultimate proof for the existence of rafts, they have been advocated in relation with their potential influence on biological cellular processes. It has been suggested that rafts act as organizing centers for the assembly of signaling molecules, influencing membrane fluidity, and regulating receptor trafficking [9, 10].

A theoretical model for domain-induced budding of planar membranes was proposed by Lipowsky [11] some years ago, and later was extended for closed vesicles [12, 13]. In the model, the competition between the membrane bending energy and domain line tension leads to a budding transition. More recently, a model describing domain-induced budding in bilayers composed of a binary mixture of lipids was proposed by us [14]. In particular, we have shown that dimpled domains are formed and remain stable due to an asymmetry between the two compositions of the corresponding domain leaflets, given that the line tension along the domain rim is not too large. The calculations in Ref. [14] were done for a specific case where the relative concentration between the two lipids on the bilayer domain stays constant, while the lipids are allowed to freely exchange between the two leaflets.

In the last decade, however, techniques such as Langmuir-Blodgett or Langmuir-Schäefer have enabled

* jean.wolff@ics-cnrs.unistra.fr

† komura@tmu.ac.jp

‡ andelman@post.tau.ac.il

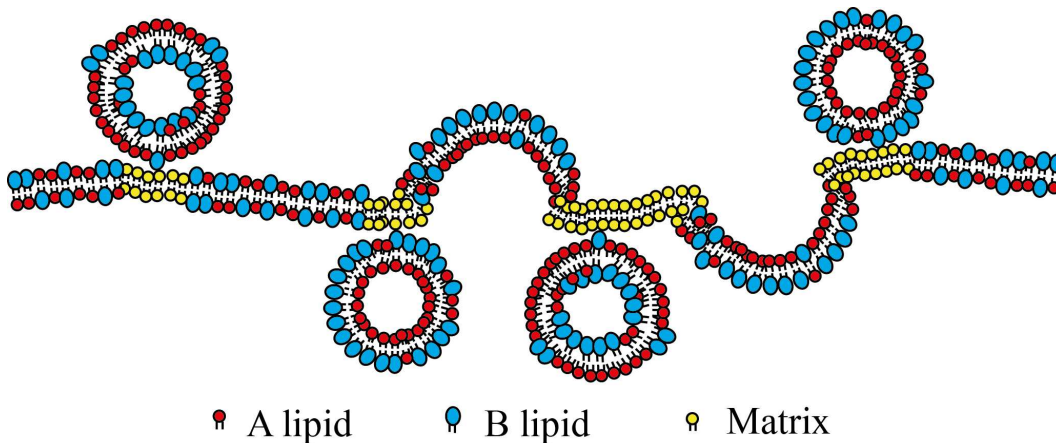


FIG. 1. Schematic vertical cut through a membrane consisting of several domains. The domains are embedded in a lipid matrix (yellow) and have a line tension acting along the domain rim. Three domain types can be seen and are further explained in Fig. 2: Flat (F), Budded (B) and Dimpled (D). Each domain is formed by two lipids (red and blue) that partition themselves differently on the two domain leaflets.

a control over the asymmetric composition of artificial membranes [15, 16]. For example, unsupported bilayers via the Montal-Müller method have been used to form asymmetric bilayers in which the composition of each leaflet was independently controlled [17]. A key ingredient in understanding those experiments is the fact that the flip-flop process that exchanges lipids across the leaflets is slower than experimental times. Given these experimental findings, it is worthwhile to consider bilayers where each of the leaflet domain composition (rather than the overall bilayer composition) can be controlled in a separate and independent way.

In this paper, we generalize our previous budding model [14] and extend it to asymmetric two-component lipid domains. Each domain leaflet has a conserved lipid composition that is independent from that of the other leaflet. We consider the possibility of domains curved in the third dimension, which can produce buds as shown in Fig. 1. In our model, the composition-dependent spontaneous curvature leads to coupling between curvature and lipid composition in each of the domain leaflets [18–20]. Such a coupling leads to rich phase behavior including various phase coexistence regions.

For the sake of clarity, we do not take into account any direct interaction between two domains that face each other, although various possibilities have been previously proposed [21]. In addition, we would like to mention that in a separate set of studies for completely planar membranes, asymmetric bilayers composed of two modulated monolayers (leaflets) were considered [22, 23]. In these works, the static and dynamic properties of concentration fluctuations have been presented together with the related micro-phase separation.

The outline of this paper is as follows. Section II generalizes our previous budding model [14], and the free-energy describing asymmetric two-component lipid do-

main is discussed. In Sec. III, we explain the conditions for various phase equilibria and how to calculate the phase diagrams. We then proceed by presenting the phase diagrams in Sec. IV, and discuss the resulting global phase behavior. Finally, a more qualitative discussion is provided in Sec. V.

II. MODEL

We consider a membrane consisting of two monolayers (the terms “monolayer” and “leaflet” will be used interchangeably in this paper), each composed of an A/B mixture of lipids, which partition themselves asymmetrically between the two leaflets. We assume that the membrane can undergo a lateral phase separation creating domains of different lipid composition. The domains are taken to fully span the two monolayers, but the leaflet compositions in these domains can be different. Hence, the formed lipid domains are, in general, asymmetric. We further assume that the two leaflet compositions are conserved and can be taken as independent from each other. In the following, we discuss the thermodynamic behavior of a system consisting of a large number of such asymmetric domains as shown in Fig. 1. For this purpose, we explain below the different terms that contribute to the domain free-energy.

In Fig. 2, we show a vertical cut through three possible domain states: flat (F), dimpled (D) and fully-budded (B). The flat circular domain (F) in (a) has an area, $S = \pi L^2$, which is assumed to remain constant during the budding process. For simplicity, we consider in (b) dimpled buds (D) whose shape is a spherical cap of radius $1/C$, and in (c) the extreme case of a completely detached spherical bud (B). The total bending energy of the budded domain is given by the curvature contribu-

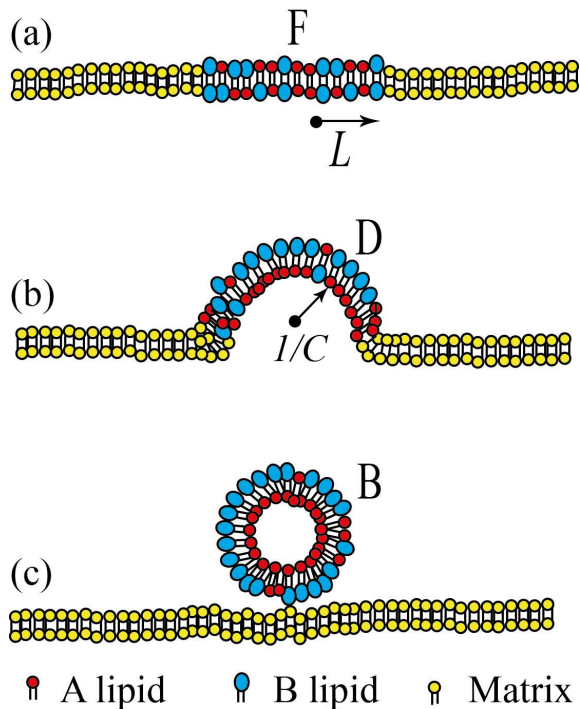


FIG. 2. A schematic vertical cut through three possible domain shapes: (a) a flat bilayer domain composed of a mixture of A and B lipids (red and blue, respectively), and embedded in an otherwise flat membrane (yellow). The circular flat domain (F) has a radius L and area $S = \pi L^2$. (b) A partial bud (dimpled domain) curved in the out-of-plane direction. The bud (D) of the same area S forms a spherical cap of radius $1/C$, where C is the curvature. (c) A fully-budded domain (B) has a spherical shape of total area S , and just touches the flat membrane. The line tension γ acts along the line boundary between the domain (red/blue lipids) and the flat membrane matrix (yellow lipids).

tions from its two monolayers [24, 25]:

$$E_{\text{bend}} = 2\pi L^2 \kappa [(C - C_0)^2 + (C + C_0)^2], \quad (1)$$

where κ is the bending rigidity modulus (assumed to be a constant that is independent of lipid composition) and C_0 the monolayer spontaneous curvature. As shown in Fig. 2, the two monolayer deform with curvatures $+C$ and $-C$, respectively.

The second energy contribution is the domain edge energy that is proportional to the perimeter length and to the line tension, γ [11]:

$$E_{\text{edge}} = 2\pi L \gamma \sqrt{1 - (LC/2)^2}. \quad (2)$$

Note that in the extreme case, when the domain buds into a complete spherical shape (B) as in Fig. 2(c), $C = \pm 2/L$ and $E_{\text{edge}} = 0$. In the above, the strong variation in composition between the domain and its surrounding matrix is effectively taken into account through the line tension, γ , which is treated as an external control parameter. This

situation can be justified for a strong segregation that results in a sharp boundary between the domain and its flat matrix surroundings.

As each domain is composed of an A/B mixture, we define ϕ_A (ϕ_B) as the area fraction (assumed to be equal to the molar fraction) of the A lipid (B lipid) in the upper leaflet domain, and similarly, ψ_A (ψ_B) for the lower leaflet domain. We assume that each monolayer is incompressible so that $\phi_A + \phi_B = 1$ and $\psi_A + \psi_B = 1$. Hence, the two relevant order parameters are the relative composition in the upper leaflet:

$$\phi = \phi_A - \phi_B, \quad (3)$$

and in the lower leaflet,

$$\psi = \psi_A - \psi_B. \quad (4)$$

As in any A/B mixture, the possibility of a phase separation can be described by a phenomenological Landau expansion of the free-energy in powers of ϕ and ψ . This expansion is done separately for each monolayer, and the total contribution to the free-energy is the sum over the two monolayers:

$$E_{\text{phase}} = \pi L^2 \frac{U}{\Xi^2} \left[\frac{t}{2}(\phi^2 + \psi^2) + \frac{1}{4}(\phi^4 + \psi^4) \right], \quad (5)$$

where $\Xi \equiv \kappa/\gamma$ is the invagination length, U is a parameter that sets the energy scale, and $t \sim (T - T_c)/T_c$ is the reduced temperature (T_c being the critical temperature). In Eq. (5) above, we multiply by the domain area, πL^2 , to obtain the domain free-energy.

Hereafter, we will use several dimensionless variables: a rescaled curvature $c \equiv LC$, rescaled spontaneous curvature $c_0 \equiv LC_0$, and rescaled invagination length $\xi \equiv \Xi/L$. The coupling between curvature and composition is taken into account by assuming a linear dependence of the spontaneous curvature c_0 on the relative composition in each of the leaflets [18–20]:

$$c_0(\phi) = \bar{c}_0 - \beta\phi, \quad (6)$$

$$c_0(\psi) = \bar{c}_0 - \beta\psi, \quad (7)$$

where \bar{c}_0 is the monolayer spontaneous curvature for the symmetric 1:1 composition, $\phi = \psi = 0$, and β is a coupling parameter that has the same value for the two monolayers. Since \bar{c}_0 is a constant, it merely shifts the origin of the chemical potential, and will be dropped out without loss of generality.

The total free-energy per domain is then given by the sum of Eqs. (1), (2) and (5): $E_{\text{tot}} = E_{\text{bend}} + E_{\text{edge}} + E_{\text{phase}}$, and its dimensionless form, $\varepsilon = E_{\text{tot}}/2\pi\kappa$, is expressed as

$$\begin{aligned} \varepsilon(\phi, \psi, c) = & (c + \beta\phi)^2 + (c - \beta\psi)^2 + \frac{1}{\xi} \sqrt{1 - c^2/4} \\ & + \frac{1}{\xi^2} \left(\frac{U}{2\kappa} \right) \left[\frac{t}{2}(\phi^2 + \psi^2) + \frac{1}{4}(\phi^4 + \psi^4) \right]. \quad (8) \end{aligned}$$

We note that Eq. (8) depends on three dimensionless parameters: β , ξ , and $U/(2\kappa)$, while the thermodynamic variables are the reduced temperature t and the three order parameters: ϕ , ψ and c . In the calculations presented hereafter, we set $U/(2\kappa) = 1$ and vary the values of β and ξ .

Within mean-field theory, the equilibrium states and phase transitions are determined by minimizing ε with respect to ϕ , ψ and c , under the condition that ϕ and ψ are conserved order parameters while c is not. From the minimization of ε with respect to c , we obtain the condition

$$2(c + \beta\phi) + 2(c - \beta\psi) - \frac{c}{4\xi\sqrt{1 - c^2/4}} = 0. \quad (9)$$

Then, by substituting the curvature $c = c(\phi, \psi)$ into Eq. (8), results in a partially minimized free-energy, ε^*

$$\varepsilon^*(\phi, \psi) = \varepsilon(\phi, \psi, c(\phi, \psi)), \quad (10)$$

as a function of ϕ and ψ .

Typical experimental values of domain sizes are in the range of $L \simeq 50\text{--}500$ nm [9], the bending rigidity $\kappa \simeq 10^{-19}\text{J}$ [25], and the line tension $\gamma \simeq 0.2\text{--}6.2 \times 10^{-12}$ J/m [26, 27]. Hence, the scaled invagination length is estimated to be in the range, $\xi \simeq 0.01\text{--}10$. These values will be used in the next section where we calculate numerically the phase diagrams.

III. PHASE EQUILIBRIA CONDITIONS

In order to obtain various phase coexistence regions, ε^* in Eq. (10) should be further minimized with respect to the conserved order parameters, ϕ and ψ . Hence, we consider the following thermodynamical potential

$$g(\phi, \psi) = \varepsilon^*(\phi, \psi) - \mu_\phi\phi - \mu_\psi\psi, \quad (11)$$

where μ_ϕ and μ_ψ are the chemical potentials coupled with the A/B relative compositions in the upper and lower domains, respectively. They act as Lagrange multipliers that take into account the conserved ϕ and ψ compositions. In general, these two chemical potentials have different values, $\mu_\phi \neq \mu_\psi$. The special case of $\mu_\phi = \mu_\psi$, for which only the total relative composition, $\phi + \psi$, is conserved was investigated in our previous work [14], while here we deal with a general situation where each of the compositions, ϕ and ψ , are conserved independently.

The thermodynamic equilibrium between the two coexisting phases denoted as ‘1’ and ‘2’ and characterized by (ϕ_1, ψ_1) and (ϕ_2, ψ_2) , satisfies the conditions [28]

$$\begin{aligned} \partial_\phi g(\phi, \psi)|_1 &= \partial_\phi g(\phi, \psi)|_2 = 0, \\ \partial_\psi g(\phi, \psi)|_1 &= \partial_\psi g(\phi, \psi)|_2 = 0, \\ g(\phi_1, \psi_1) &= g(\phi_2, \psi_2). \end{aligned} \quad (12)$$

Similarly, for a three-phase coexistence between phases ‘1’, ‘2’ and ‘3’, the following set of conditions should be

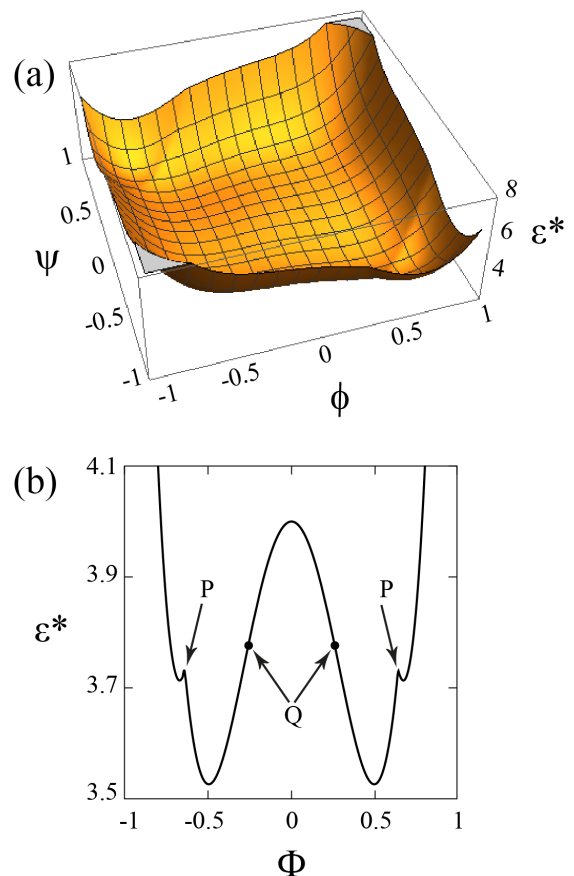


FIG. 3. (a) Plot of the partially minimized free-energy $\varepsilon^*(\phi, \psi)$ as a function of ϕ and ψ for $\xi = 0.25$, $\beta = 1$ and $t = -0.2$ (below T_c). (b) A cut through the free-energy landscape ε^* in the particular direction, $\phi + \psi = 0$, plotted as a function of $\Phi = (\phi - \psi)/2$. The two P points are cusps at which the slope of ε^* changes discontinuously, although the Hessian H remains positive (see Appendix). The two Q points correspond to the location at which H vanishes.

satisfied:

$$\begin{aligned} \partial_\phi g(\phi, \psi)|_1 &= \partial_\phi g(\phi, \psi)|_2 = \partial_\phi g(\phi, \psi)|_3 = 0 \\ \partial_\psi g(\phi, \psi)|_1 &= \partial_\psi g(\phi, \psi)|_2 = \partial_\psi g(\phi, \psi)|_3 = 0 \\ g(\phi_1, \psi_1) &= g(\phi_2, \psi_2) = g(\phi_3, \psi_3). \end{aligned} \quad (13)$$

In Fig. 3(a), we show an example of the partially minimized free-energy, $\varepsilon^*(\phi, \psi)$, as a function of ϕ and ψ at a fixed temperature $t = -0.2$ (below T_c), and for given values of ξ and β . In order to have a better view of the free-energy surface, we show in Fig. 3(b) a cross-section cut of the free-energy surface in the direction of $\Phi = (\phi - \psi)/2$, while keeping $\phi + \psi = 0$. Here, we see two singular cusps (points P) where the determinant of the Hessian matrix, H (see Appendix) does not vanish. At these cusps, H changes discontinuously although it remains positive. At points Q, on the other hand, the Hessian H vanishes. More details on the Hessian matrix and determinant, and their relation to the phase stability and

spinodal lines are presented in the Appendix. By calculation the Hessian H , it is possible to derive the spinodal lines and critical points. Note that in most cases, the critical points and spinodal will not be shown on the phase diagrams, because they are preempted by the first-order phase transition lines and coexistence regions.

The phase diagrams are obtained by further minimizing ε^* , with respect to the two independent variables, ϕ and ψ . Convex regions of the free energy correspond to single thermodynamical phases. Two-phase coexistence regions correspond to non-convex regions, where we can construct a common tangent plane. The plane touches the free-energy surface at two points that determine the two phases in coexistence. A more special three-phase coexistence region corresponds to a plane that touches the free-energy surface at three points. More details on the numerical procedure of finding the phase diagrams are given below.

The numerical computation of the phase diagram is performed using a public-domain software called ‘‘Qhull’’ [29]. The Qhull software generates initially a fine grid of triangulation, which approximates the free-energy surface, ε^* . The three-phase coexistence regions correspond to facets with all sides being much larger than the initial discretization. The two-phase coexistence regions are associated with elongated triangles having one short side that is much smaller than the other two longer sides that approximate the tie-lines. Finally, small triangular facets of the free-energy surface are associated with stable one-phase regions. The projection of the triangulated free-energy surface onto the composition plane provides a systematic approximation for the phase diagram. The Qhull results are then used as an initial condition in calculating more precisely the equilibrium phase diagrams, including the various phase coexistence, Eqs. (11)–(13).

IV. RESULTS

A. Phase diagrams

Four representative types of phase diagrams are shown in Figs. 4–7. In the first two figures, we show the calculated phase diagram for $\beta = 1$ (Fig. 4) and $\beta = 3$ (Fig. 5), while the other parameters are fixed to $\xi = 0.25$ and $t = -0.45$. The latter two phase diagrams are for $t = -0.2$ (Fig. 6) and $t = -0.02$ (Fig. 7), while keeping $\beta = 1$ and $\xi = 0.25$. For presentation purposes, in (b) of each figure, we have superimposed the color plot for the curvature c on the phase diagram presented in (a). As denoted above, the various stable phases are the fully-budded phase (B) with curvature $|c| = 2$, the dimpled or partial budded phase (D) with curvature $0 < |c| < 2$, and the flat membrane (F) with zero curvature $c = 0$. The subscripts \pm denote whether the bud is curved positively or negatively with respect to the positive normal direction of the planar membrane.

Figure 4 includes five homogeneous phases: B_{\pm} , D_{\pm}

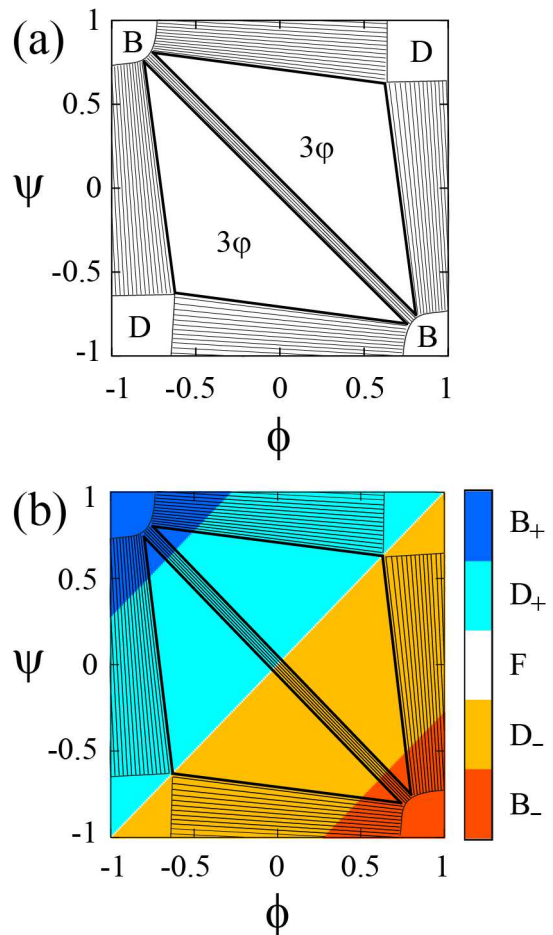


FIG. 4. (a) Phase diagram in the (ϕ, ψ) plane for $\beta = 1$, $\xi = 0.25$ and $t = -0.45$. The corners of the phase diagram indicates the four one-phases: D_{\pm} and B_{\pm} , while the flat F phase (not drawn) strictly lies only on the diagonal $\phi = \psi$. The black lines represent tie-lines in the two-phase regions, and the two triangles are the three-phase regions (see text for more details). (b) The phase diagram is plotted as in (a) but with a superimposed colored plot for the curvature, c . As one crosses the major diagonal, $\phi = \psi$, there is a smooth change from D_+ ($c > 0$) through the flat F ($c = 0$) to the D_- ($c < 0$). Furthermore, the curvature also changes smoothly inside the D_{\pm} phases, but the gradient in orange (D_-) and light blue (D_+) colors is not shown for clarity. However, the curvature has a jump between B_- ($c = -2$, red) and D_- ($-2 < c < 0$, orange) regions, as well as between B_+ ($c = 2$, dark blue) and D_+ ($0 < c < 2$, light blue) ones.

and F. The B_+ and B_- occupy the regions around the $\phi = -\psi = 1$ and $\phi = -\psi = -1$ corners, respectively. On the other hand, the D_{\pm} occupy the two remaining corners: $\phi = \psi = \pm 1$. The difference between D_+ and D_- is only associated with their curvature ($c \leq 0$), which changes continuously. This is further clarified in part (b) of the figure. For all t -values, the flat F phase (not seen on the figure) strictly exists only on the $\phi = \psi$ diagonal, but is important for the multi-phase coexistence regions

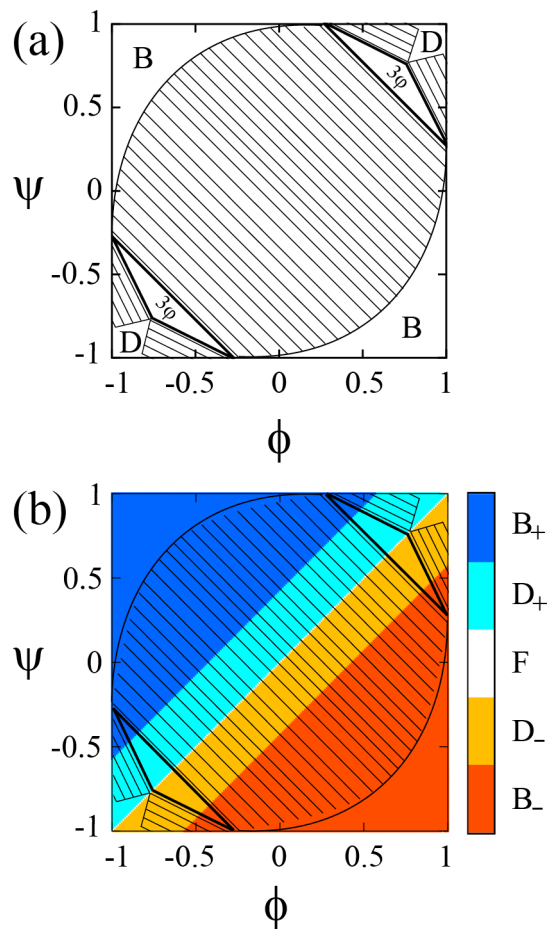


FIG. 5. (a) Phase diagram in the (ϕ, ψ) plane as in Fig. 4 but with $\beta = 3$, $\xi = 0.25$ and $t = -0.45$. (b) The phase diagram is plotted as in (a) but with a superimposed colored plot for the curvature, c .

(as discussed below). As one approaches this line from above or below, the D_{\pm} phases change-over smoothly into the F phase (with $c = 0$) on the diagonal line.

Moreover, five two-phase coexistence regions are shown in Fig. 4 together with their calculated tie-lines: two B_{+}/D_{+} and two B_{-}/D_{-} along the boundaries of the phase diagram, and one B_{+}/B_{-} along the major diagonal, $\phi = -\psi$. In addition, two three-phase coexistence regions: $B_{+}/B_{-}/F$ can be seen. These are the two triangular regions lying above and below the $\phi = -\psi$ diagonal. Note that the F corner of the three-phase region lies close to the D_{\pm} corners, but since it lies on the $\phi = \psi$ diagonal, it is identified as the F phase with $c = 0$. The three-phase coexistence region between F and B_{\pm} phases means that each point inside the triangular region is composed of three relative area fractions of the three coexisting phases: the flat (F) and budded (D_{\pm}) phases. The nearly horizontal (D_{-}/B_{-}) or vertical (D_{+}/B_{+}) tie-lines on the boundaries of phase diagram indicate that the two ϕ and ψ monolayers are almost decoupled, because either

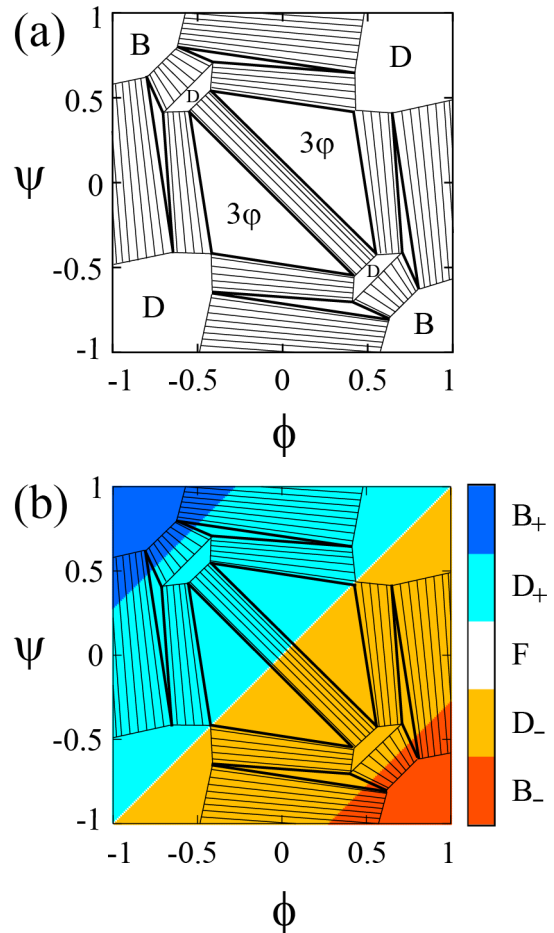


FIG. 6. (a) Phase diagram in the (ϕ, ψ) plane as in Fig. 4 but with $t = -0.2$, $\xi = 0.25$ and $\beta = 1$. (b) The phase diagram is plotted as in (a) but with a superimposed colored plot for the curvature, c .

ϕ or ψ do not vary along the tie-line. On the other hand, tie-lines that lie along the major diagonal, $\phi = -\psi$, indicate a strong coupling between the ϕ and ψ monolayers in the B_{+}/B_{-} coexistence region.

In Fig. 5 with $\beta = 3$ and the same temperature as in Fig. 4, we see that the central binary coexistence region (B_{+}/B_{-}) becomes much larger. On the other hand, the four two-phase coexistence regions of Fig. 4 have shrunken because the extent of the dimpled phase becomes smaller for larger coupling parameter, β . When β gets large values in Eqs. (6) and (7), the composition of each monolayer induces higher curvature that promotes budding. In this case, the central two-phase region, B_{+}/B_{-} , occupies a large fraction of the phase diagram, and most of its tie-lines are parallel to the diagonal $\phi = -\psi$, suggesting a strong coupling between the two monolayers. On the other hand, the two three-phase coexistence regions, $B_{+}/B_{-}/F$, become smaller in Fig. 5. Furthermore, we note that in Fig. 5(b), the regions of the dimpled phases, D_{\pm} , represented by the light blue

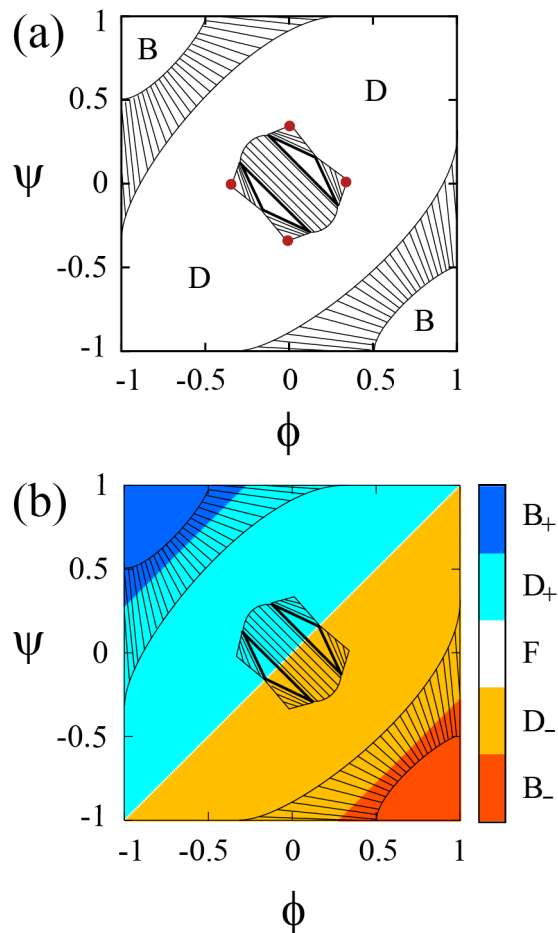


FIG. 7. (a) Phase diagram in the (ϕ, ψ) plane as in Fig. 4 but with $t = -0.02$, $\xi = 0.25$ and $\beta = 1$. The red circles correspond to the critical points. (b) The phase diagram is plotted as in (a) but with a superimposed colored plot for the curvature, c .

and orange regions are narrower as compared with those of Fig. 4(b).

It is of interest to explain how one of the monolayers induces a phase transition in the second monolayer. As an illustrative example, let us consider a point in Figs. 4 and 5 with average leaflet composition, $(\phi, \psi) = (0, -0.9)$. At these compositions, the bilayer separates in Fig. 4 into a D_- phase with compositions $(-0.75, -0.9)$ and a B_- phase with $(0.75, -0.9)$. In this weak coupling case, $\beta = 1$, the phase separation in one monolayer does not induce any instability leading towards phase separation in the second monolayer, because the tie-line is nearly parallel to the horizontal ϕ -axis. On the other hand, in Fig. 5 with a larger value of $\beta = 3$, the bilayer separates into a B_- phase with $(0.1, -0.9)$ and a B_+ phase with $(-0.9, 0.1)$. As the tie-line in this case lies along the major diagonal, $\phi = -\psi$, the two monolayers are influencing each other. Such a situation results from a strong composition-curvature coupling when the parameter β is large enough. A more general dependence of the phase

diagram on the parameter β will be further discussed in the next subsection.

Figure 6 is plotted for a higher temperature $t = -0.2$ than in Figs. 4 and 5, while we fix $\beta = 1$ as in Fig. 4. The dimpled region expands both toward the corners and the middle of the phase diagram. Moreover, there are two new one-phase regions of the dimpled phase (D_{\pm}) resulting in four additional two-phase coexistence regions: two D_+/D_+ and two D_-/D_- . The system exhibits a first-order phase transition in composition, while the transition is second-order in curvature.

In Fig. 7, the temperature is increased to $t = -0.02$, while β and ξ stay as in Fig. 4. The chosen t -value is higher than in the previous figures, and approaches the critical temperature, $t_c = 0.04$ [14]. The central region of the phase diagram is dominated by the dimpled phase (D_{\pm}), while the budded regions (B_{\pm}) exist only close to the two corners, with two-phase coexistence regions, B_+/D_+ and B_-/D_- . As seen in (b), the regions of the dimpled phases (D_{\pm}) are determined by β , and do not depend on the temperature t as long as ξ is fixed. Furthermore, there are four critical points appearing in the central region (marked by red circles), for which the system exhibits a second-order phase transition both in curvature and composition.

B. Global phase behavior

Next, we investigate how the different phase-diagram types appear and change as we adjust the system parameters in a global way. In Fig. 8, we present the global phase behavior in the $(1/\xi, \beta)$ plane for $t = -0.25$ in (a) and $t = -0.02$ in (b). We show how the four different types of phase diagrams of Figs. 4, 5, 6, 7, labelled as I, II, III and IV, respectively, evolve as function of ξ and β .

Figure 8(a) summarizes the result for $t = -0.25$ and is valid even for lower t -values. For $\beta > 2$ (strong coupling), the diagram is that of type II in which the dimpled phase (D) region shrinks while the budded phase (B) expands. For $\beta < 2$ (weak coupling), on the other hand, the diagram is mostly of type I for which the wide three-phase coexistence occurs. For $\beta < 1$ and $1/\xi < 4$, type III diagram is found, and contains coexistence regions of the dimpled phases (D_+/D_+ and D_-/D_-).

In Fig. 8(b), for $t = -0.02$ that is closer to the critical temperature, type III is replaced by type IV for $\beta < 1$ and $1/\xi < 5$, while type II also extends to smaller β when $1/\xi$ is large enough. When the temperature is higher, the phase transition in curvature from the flat (F) phase to the dimpled (D) one, becomes continuous [14].

V. DISCUSSION

In this paper, we have discussed a phenomenological model that accounts for the budding transition of asymmetric two-component lipid domains, where the two do-

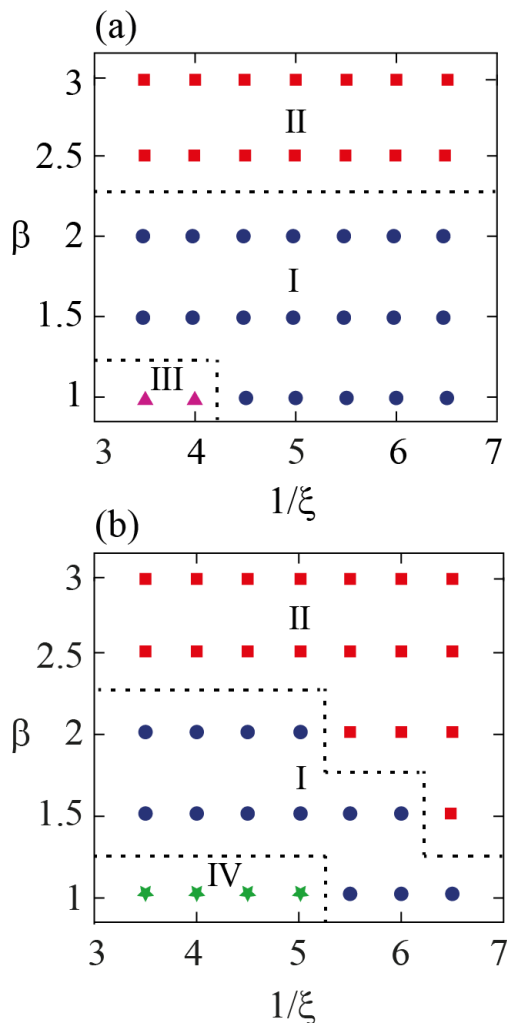


FIG. 8. Schematic phase-behavior plot in the $(1/\xi, \beta)$ plane for temperatures (a) $t = -0.25$ and (b) $t = -0.02$. The diagram types, I, II, III and IV, correspond to representative examples as in Figs. 4, 5, 6, and 7, respectively.

mains have in general different average compositions, represented by ϕ and ψ . Assuming a linear composition dependence of the spontaneous curvature, we have taken into account a coupling between the local curvature and local lipid composition in each of the two leaflets. We then explored the morphological changes between the flat and budded domains by using a thermodynamic argument. Our free-energy model contains three contributions: bending energy, accounting for domain deformation in the normal direction; line tension along the rim of the budded or flat domain; and a Landau free-energy expansion, which accounts for a phase separation of the two-component lipid domains. We have assumed, in addition, that the domain area remains constant during the budding process.

Our model predicts three different states for the domains: fully budded (B), dimpled (D), and flat (F) states.

In particular, in some ranges of parameters, the D state is found to be the most stable one, as observed in the experiment [30]. Within mean-field theory, we have calculated various phase diagrams in terms of two compositions for different temperatures t , domain size $1/\xi$, and coupling parameter, β . The resulting phase behavior is very rich. The calculated phase diagrams include various one-phase, two-phase (e.g., B_+/D_+ , B_-/D_- or B_+/B_-) and three-phase coexistence regions (e.g., $B_+/B_-/F$), depending on the curvature-composition parameter β as well as the temperature. Finally, four different types of phase diagram morphologies are found, and we have analyzed the global phase behavior in terms of the coupling parameter β , and the domain size ξ . The model analysis suggests that the asymmetry in the lipid composition between the two leaflets can lead to complex morphological and thermodynamic behavior of lipid domains.

The most important mechanism that leads to the inter-leaflet correlated phase separation, such as the two-phase coexistence seen in Fig. 5 between two budded phase (B_+/B_-), is the composition-dependent spontaneous curvature, introduced in Eqs. (6) and (7). With this mechanism, the coupling between domain curvature and its composition is controlled by the parameter β . Although we did not include any direct interaction between the domains occurring on the two leaflets, the fact that the two domains are in full registry to each other and have opposite curvatures, $\pm C$, results in a strong correlation between the opposing domains. We consider that such an effect generally exists in bio-membranes, even in the absence of specific proteins that maintain the compositional asymmetry between the two leaflets.

When the coupling parameter β is made larger at a fixed temperature (compare Figs. 4 and 5), the two-phase coexistence region, B_+/B_- , dramatically expands due to the coupling between the two leaflets. Such a strongly correlated phase separation can be in general observed for lower temperatures. We also note that the stable budded (B) phase occupies the two asymmetric corners of the phase diagram, i.e., $\phi = -\psi = \pm 1$. Moreover, the region of the dimpled (D) phase increases as the temperature is raised towards the critical temperature from below (compare Figs. 4, 6 and 7). Especially, in Fig. 7, the dimpled one-phase region dominates the central region of the phase diagram and four different critical points are expected to appear. In the intermediate temperature, as in Fig. 6, the phase diagram contains several types of two-phase coexistence regions.

The present work for asymmetric domains is a generalization of our previous model [14], where only the average composition of the domains in the two leaflets is controlled by a single chemical potential. Here, we have considered a more general situation, where each of the two domain composition is controlled in a separate and independent way. This is done by introducing two independent chemical potentials coupled to the two domain compositions, ϕ and ψ , as in Eq. (11). Hence, each domain has a conserved lipid composition that is indepen-

dent from the other one. The resulting phase diagrams show a much richer phase behavior, while the previous results [14] can be recovered by considering the special case of $\phi + \psi = \text{const.}$

Our assumption that the two opposing domains in different leaflets are correlated to each other is in accord with several experimental observations. For studies of planar but asymmetric composition in the two leaflets, Collins *et al.* [17] reported that in some cases, one leaflet can induce a phase separation in the other leaflet, depending on local lipid composition. Whereas in other cases, the two leaflets do not interact. A similar experimental phenomenon was observed for membranes composed of lipids extracted from biological cells [15]. Such situations for asymmetric membranes can be partially described by the different phase behaviors of asymmetric membrane depending on the coupling parameter β as shown in Fig. 8. Moreover, both in our model and in experiments [17], domain-induced processes take place in lipid membrane without any proteins. These results may suggest a cellular mechanism for regulating protein function by modulating the local lipid composition or inter-leaflet interactions.

Although we have mainly discussed the domain-induced budding, our model can be applied to describe the formation of vesicles in mixed amphiphilic systems [31]. It was observed in experiment that mixtures of anionic and cationic surfactants in solution form disk-like bilayers in some range of the relative amphiphile composition. As these disk-shaped bilayers grow in size, they transform into spherical caps and eventually become spherically closed vesicles. In such cases, the spontaneous curvature of bilayer membranes may be induced due to the compositional asymmetry between the two monolayers.

Acknowledgments. J.W. acknowledges support from the Service de Coopération Scientifique et Universitaire de l'Ambassade de France en Israël, the French ORT association, and ORT school of Strasbourg. S.K. acknowledges support from the Grant-in-Aid for Scientific Research on Innovative Areas “*Fluctuation and Structure*” (Grant No. 25103010) from the Ministry of Education, Culture, Sports, Science, and Technology of Japan, and the Grant-in-Aid for Scientific Research (C) (Grant No. 15K05250) from the Japan Society for the Promotion of Science (JSPS). D.A. acknowledges the hospitality of the KITPC and ITP, Beijing, China, and partial support from the Israel Science Foundation (ISF) under Grant No. 438/12, the United States–Israel Binational Science Foundation (BSF) under Grant No. 2012/060, the ISF-NSFC joint research program under Grant No. 885/15, and a CAS President’s International Fellowship Initiative (PIFI, China).

Appendix: The Hessian and Stability Analysis

In order to discuss the stability of the free-energy, we consider the 2×2 Hessian matrix of $\varepsilon^*(\phi, \psi)$ given by

$$\mathbf{H} = \begin{pmatrix} \partial_{\phi\phi}\varepsilon^* & \partial_{\phi\psi}\varepsilon^* \\ \partial_{\psi\phi}\varepsilon^* & \partial_{\psi\psi}\varepsilon^* \end{pmatrix}, \quad (\text{A.1})$$

where $\partial_{ij}\varepsilon^*$ are the second-order partial derivatives of ε^* . We recall that by minimizing $\varepsilon(\phi, \psi, c)$ with respect to c , we obtained ε^* as in Eq. (10). This leads to $\partial_c\varepsilon = 0$, $\partial_\phi\varepsilon^* = \partial_\phi\varepsilon$, and $\partial_\phi c = -\partial_{c\phi}\varepsilon/\partial_{cc}\varepsilon$, as well as similar expressions for the ψ derivatives. Using these relations, one can show that the components of \mathbf{H} are given by

$$\begin{aligned} \partial_{\phi\phi}\varepsilon^* &= \partial_{\phi\phi}\varepsilon - \frac{(\partial_{c\phi}\varepsilon)^2}{\partial_{cc}\varepsilon}, \\ \partial_{\psi\psi}\varepsilon^* &= \partial_{\psi\psi}\varepsilon - \frac{(\partial_{c\psi}\varepsilon)^2}{\partial_{cc}\varepsilon}, \\ \partial_{\phi\psi}\varepsilon^* &= \partial_{\psi\phi}\varepsilon^* = \partial_{\phi\psi}\varepsilon - \frac{(\partial_{c\phi}\varepsilon)(\partial_{c\psi}\varepsilon)}{\partial_{cc}\varepsilon}. \end{aligned} \quad (\text{A.2})$$

At the spinodal condition, the Hessian defined as the determinant of the matrix, $H = \det \mathbf{H}$, vanishes. This condition can be written as

$$\begin{aligned} &\left[2\beta^2 + \frac{1}{\xi^2}(t + 3\phi^2) - \frac{4\beta^2}{\partial_{cc}\varepsilon} \right] \\ &\times \left[2\beta^2 + \frac{1}{\xi^2}(t + 3\psi^2) - \frac{4\beta^2}{\partial_{cc}\varepsilon} \right] - \frac{16\beta^4}{(\partial_{cc}\varepsilon)^2} = 0, \end{aligned} \quad (\text{A.3})$$

where

$$\partial_{cc}\varepsilon = 4 - \frac{1}{4\xi(1 - c^2/4)^{3/2}}. \quad (\text{A.4})$$

The critical point can be derived by considering another 2×2 matrix

$$\mathbf{H}' = \begin{pmatrix} \partial_{\phi\phi}\varepsilon^* & \partial_{\phi\psi}\varepsilon^* \\ \partial_{\phi}H & \partial_{\psi}H \end{pmatrix}, \quad (\text{A.5})$$

and its determinant $H' = \det \mathbf{H}'$. One can explicitly show that

$$\begin{aligned} \partial_{\phi}H &= (\partial_{\phi\phi\phi}\varepsilon^*)(\partial_{\psi\psi}\varepsilon^*) - (\partial_{\phi\psi}\varepsilon^*)(\partial_{\phi\phi\psi}\varepsilon^*) \\ &+ (\partial_{\phi\phi}\varepsilon^*)(\partial_{\phi\psi\psi}\varepsilon^*) - (\partial_{\phi\phi\psi}\varepsilon^*)(\partial_{\phi\psi}\varepsilon^*), \end{aligned} \quad (\text{A.6})$$

$$\begin{aligned} \partial_{\psi}H &= (\partial_{\phi\phi\psi}\varepsilon^*)(\partial_{\psi\psi}\varepsilon^*) - (\partial_{\phi\psi}\varepsilon^*)(\partial_{\phi\psi\psi}\varepsilon^*) \\ &+ (\partial_{\phi\phi}\varepsilon^*)(\partial_{\psi\psi\psi}\varepsilon^*) - (\partial_{\phi\psi\psi}\varepsilon^*)(\partial_{\phi\psi}\varepsilon^*). \end{aligned} \quad (\text{A.7})$$

Then, the conditions for the critical point are given by [28]

$$H = 0 \quad \text{and} \quad H' = 0. \quad (\text{A.8})$$

-
- [1] P. F. Devaux and R. Morris, *Traffic* **5**, 241 (2004).
- [2] G. van Meer, F. R. Voelker, and G. W. Feigenson, *Nat. Rev. Mol. Cell.* **9**, 112 (2008).
- [3] J. A. F. Op den Kamp, *Annu. Rev. Biochem.* **48**, 47 (1979).
- [4] P. F. Devaux, *Biochemistry* **30**, 1163 (1991).
- [5] T. Pomorsky, R. Lombardi, H. Riezman, P. F. Devaux, G. van Meer, and J. C. Holthuis, *Mol. Biol. Cell.* **14**, 1240 (2003).
- [6] D. L. Daleke, *J. Biol. Chem.* **282**, 821 (2007).
- [7] D. L. Daleke, *J. Lipid Res.* **44**, 233 (2003).
- [8] See e.g., S. Komura and D. Andelman, *Adv. Colloid Interface Sci.* **208**, 34 (2014), and references therein.
- [9] K. Simons and E. Ikonen, *Nature* **387**, 569 (1997).
- [10] S. Munro, *Cell* **115**, 377 (2003).
- [11] R. Lipowsky, *J. Phys. II (France)* **2**, 1825 (1992).
- [12] F. Jülicher and R. Lipowsky, *Phys. Rev. Lett.* **70**, 2964 (1993).
- [13] F. Jülicher and R. Lipowsky, *Phys. Rev. E* **53**, 2670 (1996).
- [14] J. Wolff, S. Komura, and D. Andelman, *Phys. Rev. E* **91**, 012708 (2015).
- [15] V. Kiessling, J. M. Crane, and L. K. Tamm, *Biophys. J.* **91**, 3313 (2006).
- [16] H.-T. Cheng, Megha, and E. London, *J. Biol. Chem.* **284**, 6079 (2009).
- [17] M. D. Collins and S. L. Keller, *Proc. Natl. Acad. Sci. USA* **105**, 124 (2008).
- [18] S. Leibler and D. Andelman, *J. Phys. (France)* **48**, 2013 (1987).
- [19] S. A. Safran, P. Pincus, and D. Andelman, *Science* **248**, 354 (1990).
- [20] F. C. MacKintosh and S. A. Safran, *Phys. Rev. E* **47**, 1180 (1993).
- [21] S. May, *Soft Matter* **5**, 3148 (2009).
- [22] Y. Hirose, S. Komura, and D. Andelman, *ChemPhysChem* **10**, 2839 (2009).
- [23] Y. Hirose, S. Komura, and D. Andelman, *Phys. Rev. E* **86**, 021916 (2012).
- [24] W. Helfrich, *Z. Naturforsch. C* **28**, 693 (1973).
- [25] S. A. Safran, *Statistical Thermodynamics of Surfaces, Interfaces, and Membranes*, (Addison Wesley, Reading, 1994).
- [26] T. Baumgart, S. T. Hess, and W. W. Webb, *Nature* **425**, 821 (2003).
- [27] A. Tian, C. Johnson, W. Wang, and T. Baumgart, *Phys. Rev. Lett.* **98**, 208102 (2007).
- [28] J. W. Gibbs, *The Scientific Papers of J. Willard Gibbs, volume 1, Thermodynamics* (Longmans, Green, and Co., London, 1993).
- [29] C. Barber, D. Dobkin, and H. Huhdanpaa, *ACM Trans. Math. Softw.* **22**, 469 (1996).
- [30] J. E. Rim, T. S. Ursell, R. Phillips, and W. S. Klug, *Phys. Rev. Lett.* **106**, 057801 (2011).
- [31] A. Shioi and T. A. Hatton, *Langmuir* **18**, 7341 (2002).